PAPER • OPEN ACCESS

Impact of atomic defects in the electronic states of FeSe$_{1-x}$S$_x$ superconducting crystals

To cite this article: Jazmín Aragón Sánchez *et al* 2022 *J. Phys. Mater.* **5** 044008

View the article online for updates and enhancements.

Journal of Physics: Materials

PAPER

Impact of atomic defects in the electronic states of FeSe$_{1-x}$S$_x$ superconducting crystals

Jazmín Aragón Sánchez[1,2,3], María Lourdes Amigó[1,2], Cristian Horacio Belussi[1,2],
María Victoria Ale Crivillero[2,4], Sergio Suárez[2], Julio Guimpel[1,2], Gladys Nieva[1,2], Julio Esteban Gayone[1,2]
and Yanina Fasano[1,2,3,*] (ORCID)

1 Instituto de Nanociencia y Nanotecnología, CNEA and CONICET, Nodo Bariloche, Avenida Bustillo 9500, 8400 Bariloche, Argentina
2 Centro Atómico Bariloche and Instituto Balseiro, CNEA and Universidad Nacional de Cuyo, Avenida Bustillo 9500, 8400 Bariloche, Argentina
3 Leibniz Institute for Solid State and Materials Research, Helmholtzstraße 20, 01069 Dresden, Germany
4 Max-Planck-Institute for Chemical Physics of Solids, Nöthnitzer Straße 40, 01187 Dresden, Germany
* Author to whom any correspondence should be addressed.

E-mail: yanina.fasano@cab.cnea.gov.ar

Abstract

The electronic properties of Fe-based superconductors are drastically affected by deformations on their crystal structure introduced by doping and pressure. Here we study single crystals of FeSe$_{1-x}$S$_x$ and reveal that local crystal deformations such as atomic-scale defects impact the spectral shape of the electronic core level states of the material. By means of scanning tunneling microscopy we image S-doping induced defects as well as diluted dumbbell defects associated with Fe vacancies. We have access to the electronic structure of the samples by means of x-ray photoemission spectroscopy (XPS) and show that the spectral shape of the Se core levels can only be adequately described by considering a principal plus a minor component of the electronic states. We find this result for both pure and S-doped samples, irrespective that in the latter case the material presents extra crystal defects associated to doping with S atoms. We argue that the second component in our XPS spectra is associated with the ubiquitous dumbbell defects in FeSe that are known to entail a significant modification of the electronic clouds of surrounding atoms.

1. Introduction

The so called iron age of high-temperature superconductivity renewed the hope on discovering superconducting compounds with technically relevant critical temperatures. This age was inaugurated by the discovery of superconductivity with a critical temperature $T_c = 26$ K in the superconductor LaO$_{1-x}$F$_x$FeAs [1] and was followed by numerous reports of superconductivity in the Fe-based superconductors family [2–6]. Among all the members of this family, the FeSe compound [2] has attracted much attention since it has a simple crystal structure of stacks of superconducting layers and its T_c can be enhanced up to 37 K by applying hydrostatic pressure [7, 8], the largest value for a binary compound.

In addition, FeSe is special since puzzles the understanding of the nature of high-temperature superconductivity in Fe-based superconductors: while most of them presents a magnetic order that seems to be in close relationship with superconductivity [9, 10], in FeSe no static magnetic order is observed at ambient pressure [10–12]. This compound also presents a tetragonal to orthorhombic transition on cooling around 90 K [13] without undergoing any magnetic transition [14, 15]. Another relevant part of the puzzle is that doping FeSe with chalcogen atoms or applying pressure produces significant changes in the phase diagram of the compounds [16] and enhances magnetic instability [17]. Indeed, spectroscopic data obtained by means of scanning tunneling microscopy (STM) give support to the idea that spin fluctuations have a relevant role in the superconducting pairing mechanism of Fe-based superconductors [18–20]. All these results indicate that in FeSe there is an intricate interplay between the crystal structure and electronic properties such as superconductivity and magnetism.

For instance, introducing chemical pressure in the material by isovalently substituting Se with another chalcogen element is a suitable control parameter to tune crystal structure deformations [21] as well as the critical temperature [16]. Other examples of the fine interplay between crystal structure and electronic properties in FeSe is the radical enhancement of T_c when growing strained monolayer films on top of $SrTiO_3$ substrates [22], or when coating the samples with K adatoms [23]. Atomic-scale local crystal structure modifications such as defects do also play a role in the electronic and superconducting properties of the material [1, 24]. A prominent example of this is reported in molecular beam epitaxy (MBE)-grown FeSe films presenting dumbbell-type atomic defects: superconductivity is suppressed on tuning the defect concentration above a relatively low critical value [25]. Thus, understanding the impact of atomic-scale defects in the electronic structure of Fe-based superconductors is of key importance for assessing how critical is the occurrence of these features for the establishment of superconductivity in these compounds.

With the aim of studying this impact, here we study single crystals of $FeSe_{1-x}S_x$, the Fe-based compound with the simplest crystal structure, consisting of a stack of superconducting layers. We apply STM to reveal that this compound presents S-doping induced defects as well as diluted dumbbell defects associated with an Fe vacancy. We measure the electronic structure of the samples by means of x-ray photoemission spectroscopy (XPS) and reveal that the spectral shape of the peaks of some of the Se and Fe core levels can only be adequately described by considering a dominant plus a smaller second component of the electronic states. We find this result for both, pure as well as S-doped samples, irrespective that they present extra crystal defects associated with the substitution of Se by S atoms. Structural and resistivity characterization, as well as the spectral shape and energy location of the peaks in XPS spectra, indicate our samples do not present inter-growths of the hexagonal phase. Even though in our STM topographies only ~4% of the imaged Se atoms are involved in dumbbell defects, according to DFT calculations these defects entail a significant modification of the electronic clouds of the eight Se and Fe atoms surrounding the Fe vacancy. Thus, we suggest the second component in our XPS spectra is associated with the ubiquitous dumbbell defects in FeSe. This impact of the atomic defects in the binding energy and the spectral shape of the core levels in $FeSe_{1-x}S_x$ highlights the subtle interplay between the crystal structure and the bulk electronic states in Fe-based superconductors.

2. Experimental details and characterization of samples

In this work we study platelet-like $FeSe_{1-x}S_x$ single crystals obtained by means of the vapor transport method. Crystals were grown during 45 days using a $KCl: 2AlCl_3$ flux and a temperature-gradient with a hot-point of 395 °C and a cold-point of 385 °C. Further details on the crystal growing method can be obtained in [26]. X-ray diffraction experiments at room temperature indicate the single crystallinity and the tetragonal structure of the samples and do not show any detectable trace of spurious phases [26]. We have not detected a significant concentration of Al nor K neither with energy-dispersive x-ray spectroscopy nor with time-of-flight secondary ion mass spectrometry techniques. The XPS spectra measured in our samples show no peaks that could be associated with the K 2p doublet nor Al 2s and Al 2s levels. Thus, no significant concentration of Al and K from the growing flux is detected in our samples.

Figure 1(a) presents the *ab*-plane normalized resistivity, $\rho_N = \rho(T)/\rho(200\,K)$, of the studied single crystals. As shown in the insert, the single crystals present superconducting transitions with $T_c = 9.6(0.2)\,K$ for $x = 0$, and $10(0.2)\,K$ for the S-doped sample, both with transition width of 2 K. An increase of the superconducting critical temperature is expected in the latter due to the positive chemical pressure introduced by the S-dopant atoms [16].

Data in figure 1(a) show that the resistivity ρ_N of the crystals present a kink at an intermediate temperature. This feature is associated with the structural transition from tetragonal to orthorhombic symmetry on cooling, occurring at $T_s \sim 90\,K$ for pure FeSe according to elastic neutron scattering measurements [27]. This transition temperature T_s is manifested as a departure of the resistivity from its high-temperature linear behavior [27]. This temperature coincides with the midpoint of the jump in $d\rho_N(T)/dT$ as indicated in the insert to figure 1(b). Following this criteria we found $T_s = 89(1)\,K$ for our $x = 0$ and $85(1)\,K$ for our S-doped single crystals, see dashed lines. This last value is in agreement with a doping range $x = 0.02–0.03$ according to the literature [16].

We would like to point out that the temperature location and shape of the kink in the derivative of $d\rho_N(T)/dT$ associated with the tetragonal to orthorhombic transition seems to be a good criteria to ascertain the purity and crystallographic quality of $FeSe_{1-x}S_x$ samples [11, 27]. For comparison, in figure 1 we show data for a crystal from another batch with formula $Fe_{0.92}Se$ [26] and for a sputtered $FeSe/SrTiO_3$ film [28], both presenting inter-growths of the magnetic hexagonal phase. This film has a tweed grain pattern with a typical length scale ~1 μm. In the case of the Fe-deficient crystal the kink in resistivity and jump in its derivative is fainted and a $T_s \sim 75\,K$ can be estimated. This decrease in the structural transition temperature
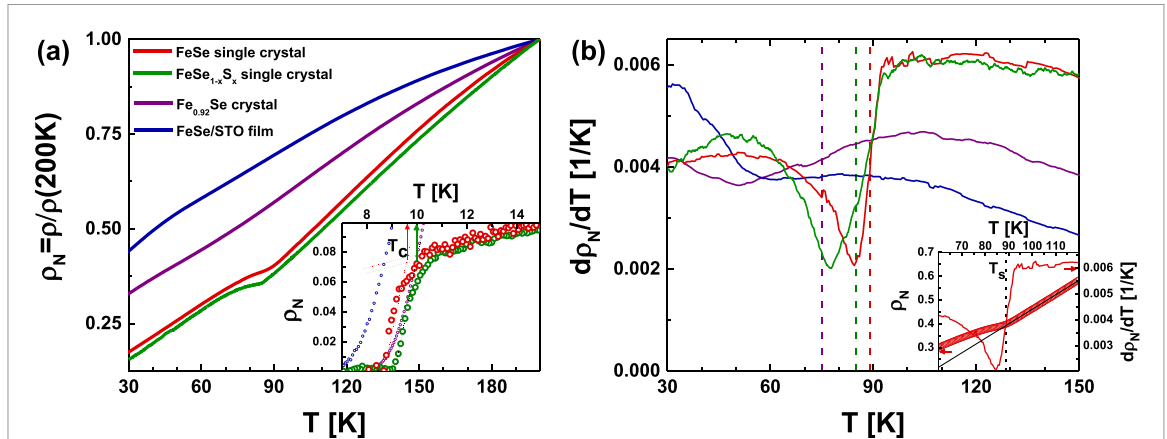
Figure 1. Transport properties of FeSe$_{1-x}$S$_x$ single crystals. (a) Normalized resistivity $\rho_N = \rho(T)/\rho(200\,\mathrm{K})$ in the intermediate temperature range for the pure and S-doped single crystals studied in this work (red and green points). We also compare data in single crystals with data in a FeSe crystal with inter-growths of spurious phases (violet points) and with data in a FeSe/STO film with important mosaicity (blue points). Insert: detail of the superconducting transition of the single crystals at low temperatures with the superconducting critical temperature T_c indicated with arrows. (b) Derivative of the normalized resistivity with respect to temperature for the curves in panel (a). The tetragonal to orthorhombic transition temperature T_s is indicated with dashed vertical lines. Insert: criteria used to estimate T_s from the resistivity and its derivative.
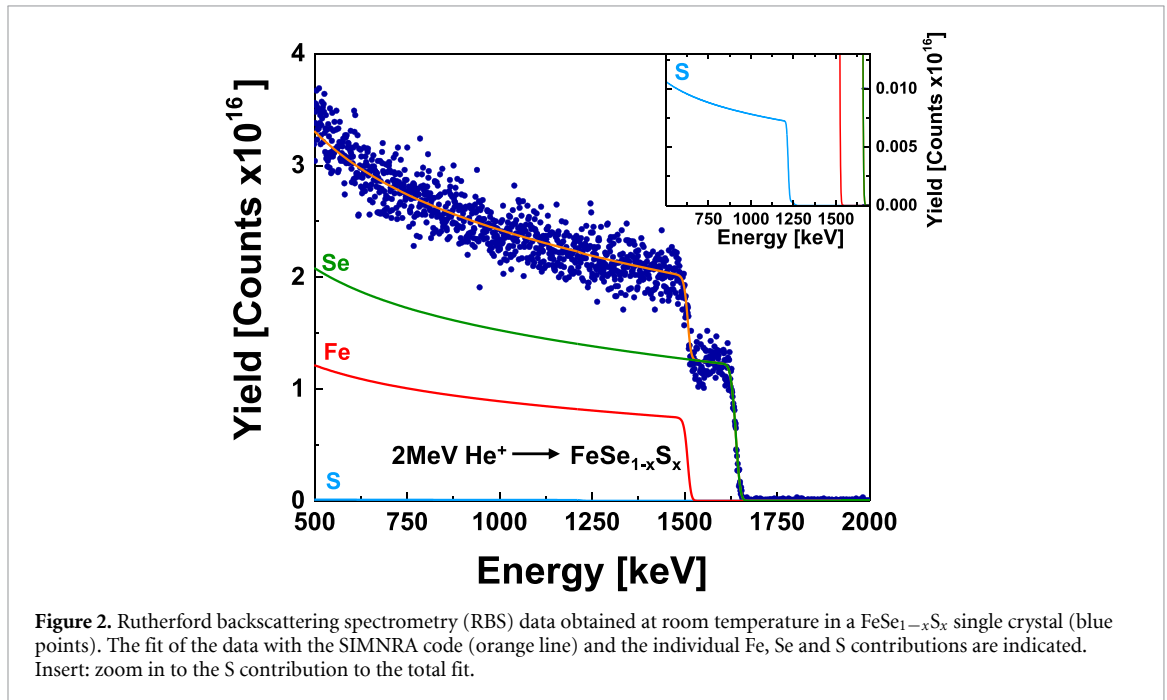
Figure 2. Rutherford backscattering spectrometry (RBS) data obtained at room temperature in a FeSe$_{1-x}$S$_x$ single crystal (blue points). The fit of the data with the SIMNRA code (orange line) and the individual Fe, Se and S contributions are indicated. Insert: zoom in to the S contribution to the total fit.

is also found in Se-deficient crystals [13]. In the case of the FeSe film with strong mosaicity the minimum in $d\rho_N(T)/dT$ is not even evident. Thus, we argue that the single crystalline samples we study in this work have a good crystal quality as ascertained by transport measurements.

We measured the level of S-doping in our samples by means of bulk and surface sensitive techniques. In the first case, x-ray energy-dispersive spectroscopy yields a bulk composition of $x = 0.03(0.01)$. The level of S was also estimated by means of Rutherford backscattering spectrometry (RBS) measurements performed using a 1.7 MV Tandem particle accelerator and irradiating the sample with 2 MeV He ions. This technique is sensitive to the S composition in a surface layer of roughly 1 μm. The RBS data presented in figure 2 are fitted with the SIMNRA code developed for the simulation of RBS and other spectra [29]. The total fit of the spectra is shown with an orange line and the contributions of the different elements are indicated with color lines. This fitting yields a S doping level of $x = 0.04(0.02)$. We also estimated the local concentration of S at the top layer of *in-situ* cleaved samples by means of STM. We found in the exposed surfaces an average value of $x = 0.027(0.005)$.

In order to study the electronic states in our FeSe$_{1-x}$S$_x$ single crystals, we applied STM and XPS techniques. STM data were obtained with a variable-temperature scanning tunneling microscope from

Omicron Nanotechnology allowing cooling the sample down to ∼30 K by means of a cold-finger connected to a continuous He-flux refrigeration system. Topographies were obtained in constant-current mode with tunneling regulation conditions in the ranges of 0.2–0.8 V and 0.7–1.3 nA. Typically, we observed images with atomic resolution when scanning at a speed between 30 and 40 nm s^{-1}. XPS measurements were performed in a system for surface analysis from SPECS. The main chamber, with a base pressure in the low 10^{-10} Torr range, is equipped with a high-resolution energy analyzer and a monochromatic Al_{K_α} x-ray source (1486.4 eV). The spot size of the XPS system is of few millimeters and the samples have 1 mm^2 of area at maximum. Thus we are inevitably collecting signal coming from the sample holder and epoxy used to glue the sample.

3. Results

Figures 3(a) and (b) show examples of STM current-constant topography images of the UHV *in-situ* cleaved FeSe$_{1-x}$S$_x$ crystals studied in the tetragonal phase (normal state). The intensity of every pixel of this image entails local information on the electronic properties of the material since corresponds to an integration of the local electron density of states of the sample up to the regulation voltage of the junction. The images present bright spots arranged in a two-dimensional square lattice. The crystal structure of the FeSe system is composed of a stack of Fe planes with Se atoms located a distance $z_{Se} = 1.47$ Å [14] above and below the plane, see schematic of figure 3. The easy cleaving plane of the samples is located between two adjacent Se planes. Thus, when cleaving the sample, the Se atoms located above the top Fe plane are exposed, see atoms highlighted in green in the schematic crystal structure of figure 3(e). Therefore the bright spots in the topographic image correspond to Se atoms spaced a distance *a* for the tetragonal phase, see arrows in panel (a). Both in the case of pure or S-doped single crystals this separation is in average 3.8(0.1) Å, in agreement with the value reported in the literature for the lattice spacing $a = 3.77$ Å [13].

The topographic images for both types of samples show a ubiquitous feature: pairs of brighter Se atoms aligned in the **a** directions indicated with dashed-white frames in figures 3(a) and (b). These brighter atoms are observed as higher atomic peaks in traces of profile height as the one shown in figure 3(c). Statistics in all our topographic images indicate the height difference in brighter atomic peaks with respect to the surrounding atoms is of 0.4(0.1) Å in pure FeSe and 0.4(0.3) Å in S-doped samples. The distribution of these features is quite diluted, representing 4.2(0.6) and 3.8(0.6)% of the STM-imaged Se atoms in the pure and S-doped samples respectively. Statistics were performed considering 1500 atoms in the case of pure FeSe and 5000 atoms in the case of S-doped samples. These features were also reported in STM topographic studies of *in-situ* MBE-grown FeSe films [30] and are also observed in studies of FeSe crystals by other authors [31]. According to a previous report in the literature, *in-situ* grown FeSe films are no longer superconducting if a large density of Se atoms imaged at the sample surface are entailed in these features [30].

By means of density functional theory simulations, the authors of [30] showed that this brighter atoms are dumbbell defects associated with an Fe vacancy in the site in between the two brighter Se atoms. The schematic of figure 3(f) shows that this defect generates a modification of the electronic cloud of the 2 Se atoms located above the plane and imaged as brighter by STM (orange), the 2 Se atoms located below (magenta), and the 4 first-neighbor Fe atoms (turquoise). The schematic of the charge density isosurfaces in the plane, shown in the right column of the figure, highlights the asymmetry in the shape of the electronic cloud of these 8 atoms with respect to the symmetric ones expected for atoms located further away from the defect (4 Fe atoms with red clouds). Furthermore, the same calculations show that the missing Fe atom induces that the orbitals on the 2 Se atoms located above the plane (orange ones) protrude further out than in the case of the other Se atoms (green). Thus, since a topographic image is proportional to the integral of the local density of states up to the regulation voltage, this protrusion of the electronic cloud results in an apparent larger height (brighter spots) of the Se atoms entailed in the dumbbell defect. Even though the density of dumbbell defects imaged by STM is small, these are defects imaged only at the surface, and such defects can certainly occur in every FeSe plane of the crystal. Thus, the concomitant modification of the electronic cloud of the 8 atoms directly involved in dumbbell defects might have a small though noticeable impact in the bulk electronic properties of the samples.

In the case of the S-doped samples, another prominent feature is also imaged in several locations: local depletions of the sample height associated to darker chalcogen atoms. Height profiles along these features indicate that in the darker areas there is a height depletion of roughly 25% with respect to neighbor Se atoms, a magnitude of ∼20% the *c*-axis unit cell of the material, see for example figure 3(d). These features are not detected in measurements in pure FeSe crystals performed by us nor in works of other authors [21, 30, 31]. This type of defects were also observed in STM topographies of S-doped crystals with an occurrence that grows with the S concentration [21]. Given that S has a smaller atomic radius than Se, it can be assumed that S atoms are imaged by STM as these darker features entailing a local depletion of height.
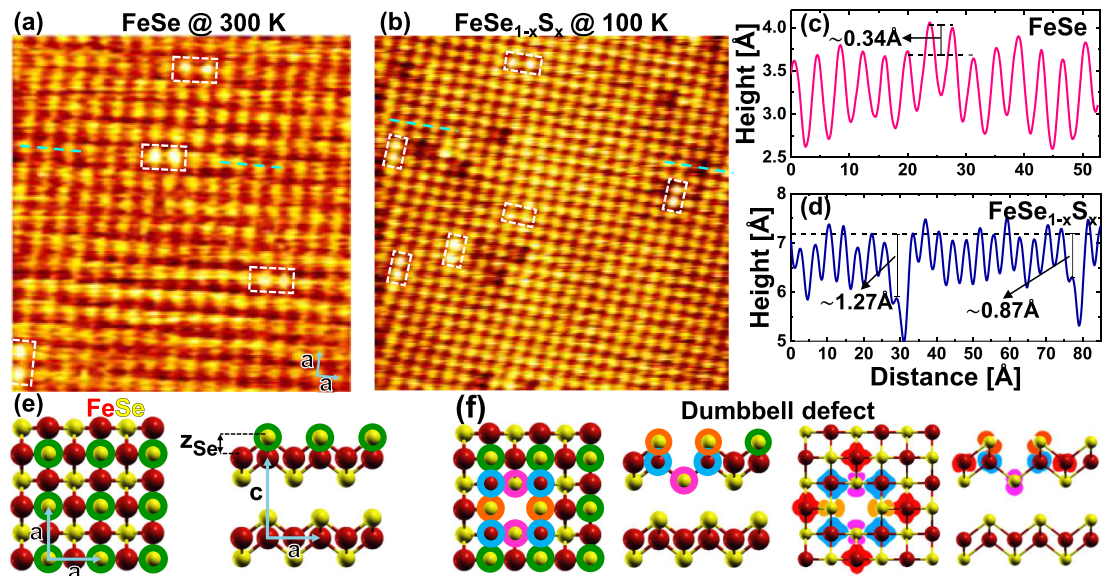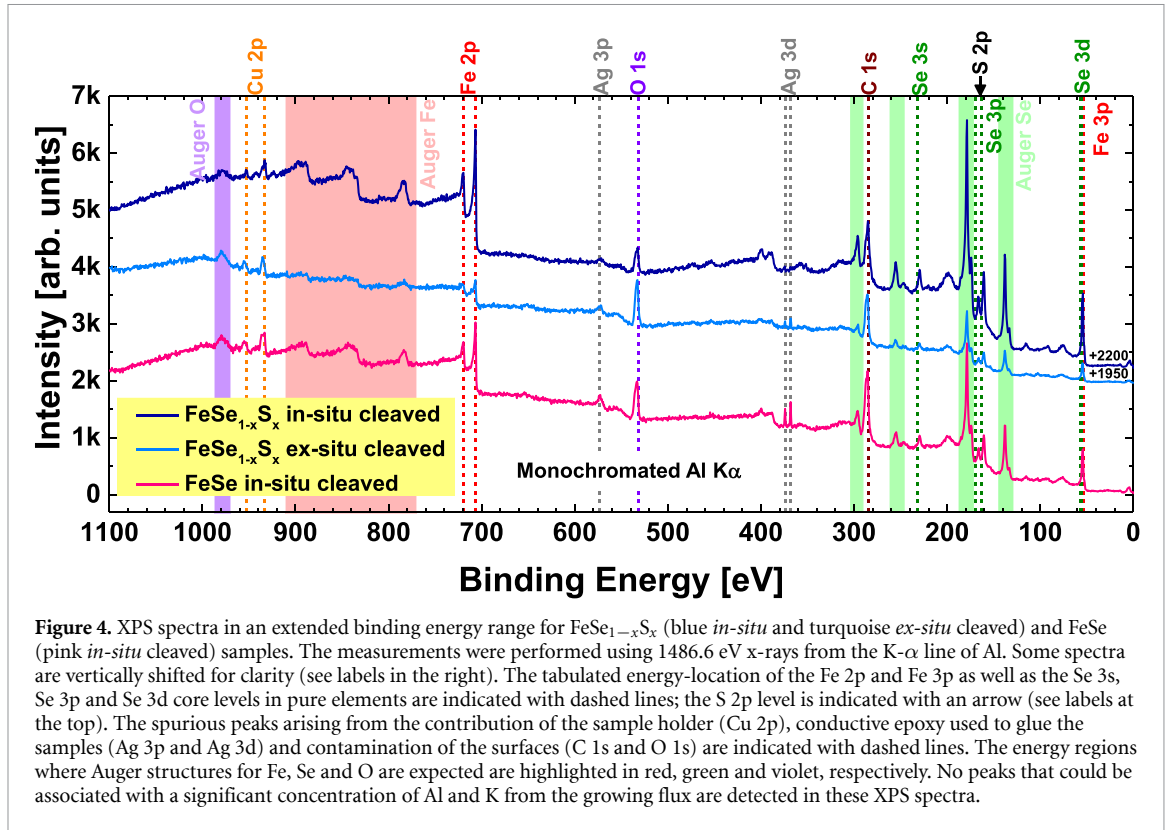
Figure 3. STM topography images and crystal structure of $FeSe_{1-x}S_x$ in the high-temperature tetragonal phase. (a) 6×6 nm^2 topography of an *in-situ* cleaved single crystal with $x = 0$. The exposed Se atoms are observed as bright spots. Dumbbell defects (see white dashed frames) are observed as two bright Se atoms oriented along the **a**-axis directions. Image acquired in constant-current mode at 0.7 nA and 0.7 V. (b) 10×10 nm^2 topography of an *in-situ* cleaved crystal with $x = 0.027(0.005)$ at the surface. Local depletions of the sample height (darker chalcogen atoms) are presumably generated by smaller S dopant atoms. Dumbbell defects are also indicated with dashed-white frames. Image acquired in constant-current mode at 1.3 nA and 0.2 V. For both samples the measured lattice spacing is $a = 3.8(0.1)$ Å. (c) Height-profile in FeSe along the trace indicated (partially) with a turquoise dashed line in panel (a). A dumbbell defect is observed as two local maxima of apparent height due to the protrusion of the Se electronic cloud entailed in this defect [30]. (d) Height-profile in the S-doped crystal along the trace indicated with the turquoise line in panel (b). Local minima in the surface height are detected in the darker height features. (e) Schematic representation of the FeSe crystal structure in the tetragonal phase. The expected $a = 3.77$ Å and $c = 5.52$ Å unit cell vectors are indicated. When cleaving the samples to perform STM measurements, the Se atoms located above the top Fe plane are imaged (highlighted in green). (f) Schematic of a dumbbell defect associated with an Fe vacancy: atomic positions (left) and charge density isosurfaces (right) of the atoms entailed in the defect. The atomic clouds of the neighboring Se and Fe atoms are schematically reproduced from the DFT calculations of [30].

Indeed, modulations of the brightness of topographic images are also observed in the $FeTe_{0.55}Se_{0.45}$ compound. In this work the darker spots are associated with the smaller atoms and the brighter ones with the larger atoms [32]. In view of this experimental evidence, our topographical data are consistent with the presence of S dopant-atoms in the darker chalcogen atom locations. Our STM results indicate that crystal disorder is more important in S-doped samples than in pure ones.

We pursue our study of the electronic properties of $FeSe_{1-x}S_x$ by means of XPS measurements that provide information on the energy spectrum of the core levels of the different elements composing the material. XPS is a surface sensitive technique, but in contrast to STM, the electronic information comes not only from the last atomic layer but also from the few atomic layers spanning a depth of ∼1 nm. Figure 4 shows the survey spectra of FeSe *in-situ* cleaved and $FeSe_{1-x}S_x$ ex and *in-situ* cleaved crystals. The *ex-situ* cleaved sample was cleaved in air right before putting it inside the preparation chamber. The spectra were obtained with an energy spacing of 0.5 eV. The collected spectra in the $FeSe_{1-x}S_x$ samples were vertically shifted for clarity. In the case of pure FeSe, our data are obtained in an *in-situ* cleaved surface of a high purity single crystal and cover a wider energy range with better signal to noise ratio and/or better energy resolution than previously reported XPS spectra [33–40]. In all spectra of figure 4, Fe and Se contributions are detected at energies close to the ones corresponding to the tabulated peaks for the different core levels for the pure elements (indicated with dotted lines) [41]. Nevertheless, the S peaks are not clearly observed since they are superimposed to the Se 3p peaks (see discussion below). Spurious Cu, Ag, O and C peaks are also detected due to the fact that the samples are smaller than the analyzed area, and we are detecting signals from the Cu sample holder and the conductive epoxy used to glue the sample. Table 1 shows a comparison of the energy location of the Fe and Se core levels tabulated for pure elements, measured in our *in-situ* cleaved $FeSe_{1-x}S_x$ single crystals and other data available in the literature for pure FeSe crystals and films.

The differences between the spectra collected in the *in-situ* and *ex-situ* cleaved samples are evident in figure 5 showing the energy range of the XPS spectra for the Fe 2p core-levels. A clear shoulder at the left of the Fe $2p_{3/2}$ peak and a faint one at the left of the Fe $2p_{1/2}$ peak are observed in the *ex-situ* cleaved $FeSe_{1-x}S_x$ surface. These shoulders appear at energies corresponding to the Fe 2p core levels tabulated for the oxidized

Figure 4. XPS spectra in an extended binding energy range for FeSe$_{1-x}$S$_x$ (blue *in-situ* and turquoise *ex-situ* cleaved) and FeSe (pink *in-situ* cleaved) samples. The measurements were performed using 1486.6 eV x-rays from the K-α line of Al. Some spectra are vertically shifted for clarity (see labels in the right). The tabulated energy-location of the Fe 2p and Fe 3p as well as the Se 3s, Se 3p and Se 3d core levels in pure elements are indicated with dashed lines; the S 2p level is indicated with an arrow (see labels at the top). The spurious peaks arising from the contribution of the sample holder (Cu 2p), conductive epoxy used to glue the samples (Ag 3p and Ag 3d) and contamination of the surfaces (C 1s and O 1s) are indicated with dashed lines. The energy regions where Auger structures for Fe, Se and O are expected are highlighted in red, green and violet, respectively. No peaks that could be associated with a significant concentration of Al and K from the growing flux are detected in these XPS spectra.

Table 1. Binding energies for the Fe and Se core levels. The first column has values tabulated for pure elements [41] but in the case of Fe3p$_{1/2}$ where the value was calculated considering the binding energy of Fe3p$_{3/2}$ and the spin–orbit coupling. The second and third columns indicate the energy location of the peaks measured in our high purity *in-situ* cleaved FeSe$_{1-x}$S$_x$ crystals. The uncertainty in the data is of 0.05 eV. We also include our estimation (from data in the figures of the corresponding papers) of the energy location of the peaks for the FeSe single crystals of [42] and MBE-grown FeSe films of [36]. Data on the energy location of the peaks in PLD-grown FeSe films provided in [40].

	Binding energy (eV)					
Species	Pure elements	FeSe this work	FeSe$_{0.97}$S$_{0.03}$ this work	FeSe crystal [42]	FeSe/MBE film [36]	FeSe/PLD film [40]
Fe2p$_{3/2}$	707	706.5	706.5	706.9	706.8	707.2
Fe2p$_{1/2}$	720.1	719.8	719.8	719.6	720.1	720.7
Fe3p$_{3/2}$	53	52.6	52.61		52.4	54.9
Fe3p$_{1/2}$	53.67	53.25	53.23			56.6
Se3p$_{3/2}$	163	160.9	160.95			
Se3p$_{1/2}$	169	166.6	166.7			
Se3d$_{5/2}$	55.6	54.15	54.15	54	54	54.48
Se3d$_{3/2}$	56.46	55.05	55.05	54.9	55	55.65

compound Fe$_2$O$_3$ [41], see dashed purple lines in the figure. This indicates that the spectra in *ex-situ* cleaved samples show extra peaks in comparison to data in *in-situ* cleaved samples, resulting from surface oxidation of the sample. In addition, for the case of both, pure and S-doped FeSe samples, notably asymmetric and sharp peaks are observed at 706.5 and 720 eV, roughly corresponding to 500 meV smaller energy values than the tabulated Fe 2p$_{3/2}$ and Fe 2p$_{1/2}$ levels of metallic Fe. This energy shift is a manifestation of the hybridization of the conducting Fe 3d levels affecting also the inner core levels, a finding previously suggested by DFT calculations [43, 44] and ultraviolet photoelectron spectroscopy data close to the Fermi level in pure FeSe [37]. The line shape and energy location of the Fe 2p peaks in our XPS spectra for *in-situ* cleaved surfaces are very similar to those measured in *in-situ* grown or Ar-sputtered surfaces of FeSe films [34, 36–40]. Peaks in the *ex-situ* cleaved sample are in contrast more rounded, as observed in data for *ex-situ* grown FeSe films [33, 34, 36, 38]. In the latter case the Fe 2p$_{3/2}$ peak is generally detected around 710 eV, the energy expected for the Fe$_2$O$_3$ oxide [33, 34, 36]. Thus, these spectral line shape and energy shifting of ∼3 eV for the Fe 2p levels are strongly affected by the sample surface preparation. The shift of XPS peaks due to spurious surface effects is an important issue to avoid in order to get information on the bulk electronic
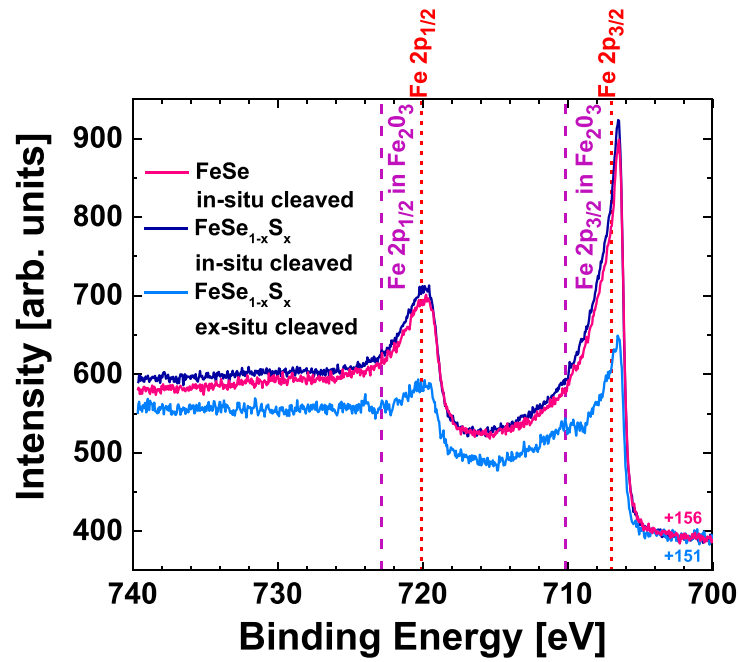
Figure 5. Detail of the Fe 2p peaks in the XPS spectra of FeSe$_{1-x}$S$_x$ (blue *in-situ* and turquoise *ex-situ* cleaved) and FeSe (pink *in-situ* cleaved) samples. For the *in-situ* cleaved samples the Fe 2p$_{3/2}$ and Fe 2p$_{1/2}$ peaks are detected at 706.5 and 719.7 eV, respectively. This energy is shifted by ∼500 meV from the expected core-level energy values for the pure elements. In the case of the *ex-situ* cleaved surface, two satellite peaks located respectively at larger binding energies than the higher ones are also observed, see purple dashed lines.
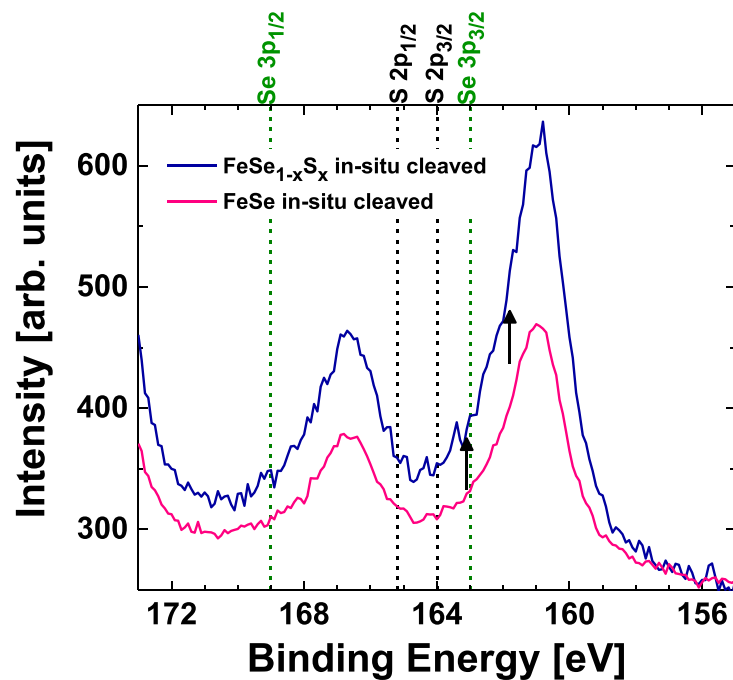

Figure 6. XPS spectra of FeSe (pink) and FeSe$_{1-x}$S$_x$ (blue) *in-situ* cleaved samples in the range of the Se 3p and S 2p levels. Dashed lines indicate tabulated values for the Se 3p$_{1/2}$, Se 3p$_{3/2}$, S 2p$_{1/2}$ and S 2p$_{3/2}$ energy core-levels of the pure elements. Arrows indicate the energy location of the S 2p peaks in a FeS crystal according to [46].

states of a sample since usually peak-shifts are expected due to hybridization. We recall that the doping of FeSe with S with $x = 0.03(0.01)$ does not produce an extra energy shift of the Fe 2p core levels.

Figure 6 shows the XPS spectra in the energy region of the Se 3p levels for the *in-situ* cleaved pure and S-doped FeSe samples. Two broad peaks centered at 160.9 and 166.6 eV are observed in both samples. According to the tabulated values for the core levels of pure elements [41], these peaks can be associated with the Se 3p doublet with a spin–orbit splitting $\Delta E \sim 6$ eV. Moreover, for both samples the observed peaks are
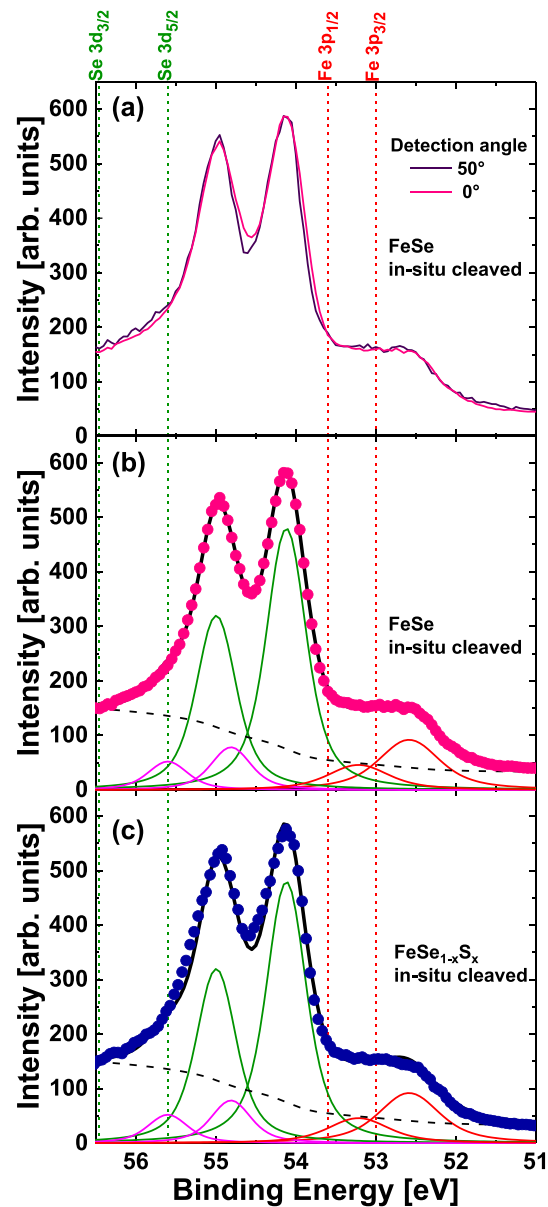
Figure 7. (a) XPS spectra in the energy region of the Se 3d and Fe3p peaks for a pure FeSe sample. Measurements performed at two different detection angles of photoemited electrons. (b) Pink points: same data than in panel (a) for a detection angle of 0 ° (normal incidence). Full black line: fit of the experimental data with a convolution of doublets of Voigt-like peaks after subtraction of a Shirley background (see black dashed line). A broad peak observed around 53 eV, close to the tabulated energy for the Fe 3p core levels, is fitted with a spin–orbit doublet (see red lines). Two pairs of peaks shown with green and magenta lines come from a principal and a minor doublet contribution associated with the Se 3d core levels. (c) Same analysis than in panel (b) for the XPS spectra measured in the S-doped crystal at normal incidence. In all panels dashed vertical lines correspond to the tabulated values for the core level energies in the pure elements.

shifted 2.1 eV for the Se $3p_{3/2}$ peak and 2.4 eV for the Se $3p_{1/2}$ peak. As in the case of the Fe 2p core levels, the energy location of the Se 3p peaks is not affected by a low doping level of S within our experimental resolution. The black dashed lines in figure 6 are located at the tabulated energy for the S 2p doublet core levels for pure elements. No local peaks above the noise level are detected at these energies nor where these peaks are reported for FeS single crystals [45], see arrows in the figure. These peaks might be difficult to detect due to, first, their expected location in a flank between the Se 3p peaks hindering the development of a faint peak due to the small amount of S in the S-doped FeSe sample. A second reason is that the photoemission cross-section of S 2p is 3 times smaller than that of Se 3p.

Figure 7 presents a detail the XPS spectra obtained for our pure and S-doped FeSe samples at the energy interval of 50–60 eV. This energy range comprises the location of the Se 3d peaks that are the highest ones, relative to the background, detected in the whole XPS spectra. For this reason, we study the spectra in this energy range to ascertain both, if there is a surface contribution, and to describe the electronic states via fits of the data. Figure 7(a) presents the XPS spectra obtained for pure FeSe samples for two different detection

angles of photoemited electrons. The shape of the measured spectra is almost independent of the detection angle within the noise level. This is a very important piece of information since it implies that the effect of the peak associated with the last-atomic-layer is negligible in our measured XPS spectra. Figures 7(b) and (c) show XPS spectra measured at normal emission for *in-situ* cleaved pure and S-doped FeSe crystals, respectively. The spectral shape in this energy range for both types of samples are alike and present no noticeable quantitative differences: two sharp peaks corresponding to the Se $3d_{5/2}$ and $3d_{3/2}$ core levels and a broad peak around 53 eV associated with the Fe $3p_{3/2}$ and Fe $3p_{1/2}$ core levels are observed as a shoulder in the low-energy flank of the Se 3d peaks.

Previously published fitting of XPS data in pure FeSe samples for this energy range do not clearly discuss the Fe 3p peak contribution [36, 39, 40, 42]. In view of the good quality of our XPS data, we study this contribution and fitted the spectra of figures 7(b) and (c) considering pairs of Voigt-like peaks after subtraction of a fitted Shirley background associated to the photoemission process of secondary electrons (see black dashed line). The corresponding spin–orbit splitting and statistical intensity ratios theoretically expected for both peaks of the doublet were left fixed in the fits. We found that a single spin–orbit doublet describes the Fe 3p levels detected at around 53 eV, see red full lines. Interestingly, the Se 3d levels are properly fitted only if considering two spin–orbit doublets indicated with green and magenta full lines. These two contributions have the same expected spin–orbit splitting and statistical intensity ratio for Se 3d levels but the energy location of the peaks are left free in the fit. The main component corresponding to the green spin–orbit doublet is centered at exactly the same energies where the peaks are detected in the experimental spectra. This component represents 86% (85%) of the area under the curve of the Se 3d peaks fit in pure (S-doped) samples. The second contribution (magenta lines) is shifted 0.64 eV toward larger binding energies with respect to the experimentally detected peaks. The consideration of these minor contribution with an area under the curve of 14% (15%) is compulsory in order to properly fit the data in both, pure and S-doped FeSe samples.

4. Discussion

The detection of quantitatively similar second contributions in the fits of the spectral shape of the Se 3d peaks in pure and S-doped crystals indicates that a significant amount of Se atoms has a different electronic environment than the rest. Since curves obtained in measurements performed at different detection angles are rather coincident, we rule out the presence of a surface peak in the Se 3d XPS spectrum. Also, since we are studying single crystals, no interface-induced changes in the electronic environment of some atoms is expected as for instance detected in amorphous films using XPS [47]. Therefore, in our case the detection of the second component is necessarily associated with local variations of charge transfer that occur in the bulk of the samples (1 nm thickness). These variations are very unlikely due to chemical inhomogeneities due to intergrowth of spurious phases: not only x-ray diffraction but also XPS data show no detectable trace of the non-superconducting hexagonal phase in our high quality crystals that was reported in other samples [42]. We can support this statement considering that the energy location of the Se 3d peaks in samples of the hexagonal non-superconducting phase are shifted toward smaller binding energies, roughly 300 meV, with respect to the position in the tetragonal FeSe phase. In contrast, the second component of the Se 3d XPS peaks are centered at larger binding energies than the maximum in the experimental data that coincides with the center of the principal component. Second, our samples present sharp Fe 2p peaks in contrast to the rounded ones that are detected in samples of the hexagonal phase, in addition are shifted 1 eV toward larger binding energies. Thus, the second component is very unlikely to have its origin in chemical inhomogeneities due to the inclusion of spurious phases in the sample.

Putting the results of the fits of XPS spectra in context with the atomic resolution images of $FeSe_{1-x}S_x$, see figure 3, we recall that crystal disorder at atomic scale is more important in S-doped samples than in pure ones. Nevertheless, the local charge transfer accounting for the second contribution does not originate in the atomic defects associated with S-doping since practically the same contributions to the fit are found in pure and S-doped samples. Thus, this type of atomic defects do not significantly affect the bulk electronic core levels of $FeSe_{1-x}S_x$ for a low doping level of $x \sim 0.03$. Our STM topographic images, as well as data from other authors [21, 30, 31], do not present evidence of a long-wavelength modulation of the topography that could be eventually associated with a spatial modulation of the chalcogen height z_{Se}.

Nevertheless, both types of samples present Fe vacancy-induced dumbbell defects detected by STM that one can reasonably assume are also present in all the FeSe planes probed by XPS. Every dumbbell defect entails changes in the electronic environment of the 4 Se atoms surrounding the Fe vacancy: according to DFT simulations of a FeSe monolayer they present a more extended electronic cloud [30]. Thus, this particular type of atomic defect have a noticeable impact in the electronic structure of $FeSe_{1-x}S_x$ and we propose that is at the origin of the second component detected in XPS spectra. The location of the doublet of

the second component in larger binding energies than the first one is in agreement with a small fraction of Se atoms having an electronic environment with less charge, quite likely induced by the smaller amount of hybridization produced by the lacking Fe atom. As for the relation between the density of Se atoms whose electronic cloud is affected ($\sim 4\%$ according to STM data) and the area under the curve of the second component of the fit (14%–15%), we would like to stress that it is possible that the Fe vacancy of a dumbbell affects the orbitals of more than 4 Se surrounding atoms. Further DFT calculations appropriately considering the van der Waals interaction and the magnetic state of the Fe atom in this compound [48] are important to quantitatively asses the possibility of the electronic cloud of more than 4 Se atoms and the z_{Se} being affected by the Fe vacancy producing the dumbbell defect. In addition, since the density of Se atoms entailed in dumbbell defects observed in topographies is obtained from statistics in a sample area of tens of nm^2, whereas XPS is probing the whole area of the sample, this difference can also come from the regions of the sample not revealed by STM having a larger concentration of dumbbell.

5. Conclusions

In conclusion, we show that STM-revealed local atomic-scale defects in the crystal structure of the simplest Fe-based superconductor have a noticeable impact in the electronic properties of the material. Indeed, a minor second component, that we argue is associated with the modification of the electronic cloud of atoms surrounding these defects, is required to properly fit the spectral shape of XPS data. Our work paves the way for future studies trying to describe the electronic properties of Fe-based superconductors by combining the atomic-scale detection of crystal deformations and the analysis of core level states via XPS probing few atomic layers. Ultimately, the results we report here on the impact of atomic defects in the binding energy and spectral shape of the core levels in FeSe$_{1-x}$S$_x$ highlights the subtle interplay between the crystal structure and the electronic states in Fe-based superconductors.

Data availability statement

The data that support the findings of this study are available upon reasonable request from the authors.

ORCID iD

Yanina Fasano ⬤ https://orcid.org/0000-0002-8658-6625

References

[1] Kamihara Y, Watanabe T, Hirano M and Hosono H 2008 *J. Am. Chem. Soc.* **130** 3296
[2] Hsu F C *et al* 2008 *Proc. Natl Acad. Sci.* **105** 14262
[3] Rotter M, Tegel M and Johrendt M 2008 *Phys. Rev. Lett.* **101** 107006
[4] Tapp J H, Tang Z, Lv B, Sasmal K, Lorenz B, Chu P C W and Guloy A M 2008 *Phys. Rev.* B **78** 060505
[5] Pitcher M J, Parker D R, Adamson P, Herkelrath S J C, Boothroyd A T, Ibberson R M, Brunelli M and Clarke S J 2008 *Chem. Commun.* 5918–20
[6] Wang X C, Liu Q Q, Lv Y X, Gao W B, Yang L X, Yu R C, Li F Y and Jin C Q 2008 *Solid State Commun.* **148** 538
[7] Margadonna S, Takabayashi Y, Ohishi Y, Mizuguchi Y, Takano Y, Kagayama T, Nakagawa T, Takata M and Prassides M 2009 *Phys. Rev.* B **80** 064506
[8] Medvedev S *et al* 2009 *Nat. Mater.* **8** 630
[9] Norman M R 2008 *Physics* **1** 21
[10] Büchner B and Hess C 2009 *Nat. Mater.* **8** 615
[11] Bohmer A E and Kreisel A 2018 *J. Phys.: Condens. Matter.* **30** 023001
[12] Chen T, Yi M and Dai P 2020 *Front. Phys.* **8** 00314
[13] Margadonna S, Takabayashi Y, McDonald M T, Kasperkiewicz K, Mizuguchi Y, Takano Y, Fitch A N, Suarde E and Prassides K 2008 *Chem. Comm.* **43** 5607
[14] McQueen T M *et al* 2009 *Phys. Rev.* B **79** 014522
[15] Bendele M, Amato A, Conder K, Elender M, Keller H, Klauss H-H, Luetkens H, Pomjakushina M, Raselli A and Khasanov R 2010 *Phys. Rev. Lett.* **104** 087003
[16] Watson M D, Kim T K, Haghighirad A A, Blake S F, Davies N R, Hoesch M, Wolf T and Coldea A I 2015 *Phys. Rev.* B **92** 121108(R)

[17] Imai T, Ahilan K, Ning F L, McQueen T M and Cava R J 2009 *Phys. Rev. Lett.* **102** 177005
[18] Fasano Y, Maggio-Aprile I, Zhigadlo N D, Katrych S, Karpinski J and Fischer Ø 2010 *Phys. Rev. Lett.* **105** 167005
[19] Hoffman J E 2011 *Rep. Prog. Phys.* **74** 124513
[20] Chi S, Grothe S, Liang R, Dosanjh P, Hardy W N, Burke S A, Bonn D A and Pennec A 2012 *Phys. Rev. Lett.* **109** 087002
[21] Hanaguri T, Iwaya K, Kohsaka Y, Machida T, Watashige T, Kasahara K, Shibauchi T and Matsuda Y 2018 *Sci. Adv.* **4** eaar6419
[22] Ge J-F, Liu Z-H, Liu C, Gao C-L, Qian D, Xue Q-K, Liu Y and Jia J-F 2014 *Nat. Mat.* **14** 285
[23] Miyata Y, Nakayama K, Sugawara K, Sato T and Takahashi T 2015 *Nat. Mat.* **14** 775
[24] Yeh K-W *et al* 2008 *Europhys. Lett.* **84** 37002
[25] Song C-L, Wang Y-L, Jiang Y-P, Li Z, Wang L, He K, Chen X, Ma X-C and Xue Q-K 2011 *Phys. Rev. B* **84** 020503(R)
[26] Amigó M L, Ale Crivillero V, Franco D G and Nieva G 2014 *J. Phys.: Conf. Ser.* **568** 022005
[27] Wang Q *et al* 2016 *Nat. Mater.* **15** 159
[28] Ale Crivillero M V, Amigó M L, Haberkorn N, Nieva G and Guimpel J 2019 *J. Appl. Phys.* **126** 115303
[29] Mayer M SIMNRA code: computer simulation of RBS, ERDA, NRA, MEIS and PIGE (available at: https://mam.home.ipp.mpg.de/)
[30] Huang D, Webb T A, Song C-L, Chang C-Z, Moodera J S, Kaxiras E and Hoffman J E 2016 *Nano Lett.* **16** 4224
[31] Putilov A V *et al* 2019 *Phys. Rev. B* **99** 144514
[32] He X, Li G, Zhang J, Karki A B, Jin R, Sales B C, Sefat A S, McGuire M A, Mandrus D and Plummer E W 2011 *Phys. Rev. B* **83** 220502(R)
[33] Feng Q J, Shen D Z, Zhang J Y, Shan C X, Lu Y M, Liu Y C and Fan X W 2004 *J. Magn. Magn. Mater.* **279** 435
[34] Wua X J, Zhanga Z Z, Zhanga J Y, Jua Z G, Shena D Z, Lia B H, Shana C X and Lua Y M 2007 *J. Cryst. Growth* **300** 483
[35] Yoshida R *et al* 2009 *J. Phys. Soc. Japan* **78** 034708
[36] Chen T-K *et al* 2010 *Thin Solid Films* **519** 1540
[37] Tsukada A, Luna K E, Hammond R H, Beasley M R, Zhao J F and Risbud S H 2011 *Appl. Phys. A* **104** 311
[38] Qi X, Wang J-Y, Kuo J-C, Yates K A and Cohen L F 2011 *J. Alloys Compd.* **509** 6350
[39] Telesca D, Nie Y, Budnick J I, Wells B O and Sinkovic B 2012 *Phys. Rev. B* **85** 214517
[40] Chaluvadi S K *et al* 2021 *Coatings* **11** 276
[41] Moulder J F, Stickle W F, Sobol P E and Bomben K D 1992 *Handbook of X-Ray Photoelectron Spectroscopy* (Minnesota: Perkin-Elmer Corporation)
[42] Yamasaki A *et al* 2010 *Phys. Rev. B* **82** 184511
[43] Subedi A, Zhang L, Singh D J and Du M H 2008 *Phys. Rev. B* **78** 134514
[44] Singh D J 2009 *Physica C* **469** 418
[45] Lai X, Zhang H, Wng Y, Wang X, Zhang X, Lin J and Huang F 2015 *Am. Chem. Soc.* **137** 32
[46] Liu C, Zhao J L, Wang J O, Qian H J, Wu R, Wang H H, Zhang N and Ibrahim K 2017 *J. Phys.: Condens. Matter* **29** 395503
[47] Guillamón I, Suderow H, Vieira S, Fernández-Pacheco A, Sesé J, Córdoba R, De Teresa J M and Ibarra M R 2008 *New J. Phys.* **10** 093005
[48] Lochner F, Eremin I M, Hickel T and Neugebauer J 2021 *Phys. Rev. B* **103** 054506